Physical Communication 27 (2018) 24–35

Contents lists available at ScienceDirect

Physical Communication

journal homepage: www.elsevier.com/locate/phycom

Full length article

Underwater acoustic communication using Doppler-resilient orthogonal signal division multiplexing in a harbor environment

Tadashi Ebihara [a,*], Geert Leus [b], Hanako Ogasawara [c]

[a] Faculty of Engineering, Information and Systems, University of Tsukuba, Tsukuba, Ibaraki 305-8573, Japan
[b] Faculty of Electrical Engineering, Mathematics and Computer Science, Delft University of Technology, Delft, Zuid-Holland 2628 CD, The Netherlands
[c] Department of Earth and Ocean Sciences, National Defense Academy, Yokosuka, Kanagawa 239-8686, Japan

ARTICLE INFO

Article history:
Received 16 April 2017
Received in revised form 5 January 2018
Accepted 5 January 2018
Available online 17 January 2018

Keywords:
Underwater acoustic communication
Delay spread
Doppler spread

ABSTRACT

Underwater acoustic (UWA) channels are one of the historical mobile ultrawideband channels characterized by large delay and Doppler spreads, but reliable UWA communication remains challenging. Here we performed an initial demonstration of the Doppler-resilient orthogonal signal division multiplexing (D-OSDM) technique in an actual sea environment. D-OSDM spreads data symbols in both time and frequency with guardbands to exploit the time and frequency diversity of UWA channels. The experiment was performed in a challenging scenario: the transmitter was fixed on a floating pier, and the receiver was mounted on a moving remote-controlled boat. The harbor UWA channel had a delay spread of 50 ms and a Doppler spread of up to 4.5 Hz, in the presence of additive Gaussian noise, and the combination of two Rayleigh fading models (a two-path model without Doppler spread and a multi-path model with Doppler spread) was able to successfully model the actual environment. Our results also confirmed that a UWA communication link using D-OSDM will deliver excellent reliability even for a harbor UWA channel with a mobile receiver; D-OSDM achieves better communication quality compared to other communication schemes in both simulations and experiments.

© 2018 Elsevier B.V. All rights reserved.

1. Introduction

Wireless communication in dynamic environments always faces delay and Doppler spreads. Such effects become dominant especially in mobile environments with fast-moving users, e.g., vehicle-to-vehicle communication [1] and mobile ultrawideband (UWB) communication [2]. Underwater acoustic (UWA) communication can be viewed as one of the historical UWB communication schemes, since it uses a large bandwidth compared to the center frequency of the signal, and because the effects of large delay and Doppler spreads are several times larger than those observed in radio communication [3]. To handle the doubly spread channels, UWA communication systems based on classical radio communication principles, such as single-carrier (SC) systems and orthogonal frequency division multiplexing (OFDM) systems, have actively been researched [4]. These systems have been used to provide a point-to-point data link between observers and subsea sensors/vehicles to explore specific points of interest [5]. However, the development of a rigid physical layer between the network terminals is still a critical issue to meet the fast-growing underwater network demand. Think for instance about the demand for large-scale exploration where a network of multiple sensors/vehicles is spread across the entire ocean in order to collect three-dimensional data or any other type of information over a wide area [6].

To provide a rigid UWA link, we proposed the use of orthogonal signal division multiplexing (hereafter referred to as normal OSDM) for UWA communication [7]. Normal OSDM spreads data symbols in the time and frequency domain similar to vector OFDM and chip-interleaved block spread code division multiple access [8,9]. It has been found that normal OSDM achieves a far better bit error rate (BER) performance compared to basic SC and OFDM systems in static UWA channels. However, it has also been demonstrated that normal OSDM is sensitive to Doppler spread, and the use of signal processing techniques for Doppler suppression is thus necessary.

To solve large delay and Doppler spreads simultaneously, we proposed Doppler-resilient OSDM (D-OSDM) [10]. D-OSDM spreads data symbols in the time domain and frequency domain with guardbands to fully exploit the time and frequency diversity of UWA channels. The successful performance of D-OSDM in a doubly spread UWA channel was demonstrated in simulations and experiments in a test tank: D-OSDM exhibited a better performance than the latest Doppler-resilient OFDM scheme (hereafter

* Corresponding author.
E-mail address: ebihara@iit.tsukuba.ac.jp (T. Ebihara).

https://doi.org/10.1016/j.phycom.2018.01.001
1874-4907/© 2018 Elsevier B.V. All rights reserved.

referred to as D-OFDM) [11]. However, no experiments have been conducted in an actual sea environment, which is inevitably more complex than that of a test tank experiment.

Herein we describe our initial demonstration of D-OSDM and normal OSDM for UWA communication in an actual mobile UWA channel. The experiment was performed in a harbor under challenging conditions; the transmitter was fixed on a floating pier, and the receiver was mounted on a moving remote-controlled boat. The performance of D-OSDM, normal OSDM and D-OFDM evaluated under such conditions can be expected to contribute to our understanding of the practical performance and effectiveness. We also determined the details of the channel characteristics and established a channel model that represents UWA communication in a harbor with a mobile receiver. We compared the simulation and experimental results to analyze how well the channel model fits the actual UWA channel.

We next provide an overview of the considered UWA communication schemes (normal OSDM and D-OSDM). The experimental setup and results are then explained in Sections 3 and 4, respectively. Section 5 describes our conclusions.

2. Overview of normal OSDM and D-OSDM

This section provides a brief overview of normal OSDM and D-OSDM. For a more detailed mathematical treatment of OSDM and D-OSDM, see [7] and [10], respectively. In the following, $\otimes$ = the Kronecker product, $\mathbb{R}^+$ = the set of positive real numbers, $\mathbb{Z}^+$ = the set of positive integer numbers, $\boldsymbol{F}_N$ = the inverse discrete Fourier transform (IDFT) matrix of size $N \times N$ and $\boldsymbol{I}_M$ = the identity matrix of size $M \times M$.

2.1. Signal processing at the transmitter and receiver

Fig. 1 is a block diagram of normal OSDM and D-OSDM at the transmitter. The transmitted signal is computed as follows:

(i) Create a data matrix (DM) of size $M \times N$ ($M, N \in \mathbb{Z}^+$), $\boldsymbol{X}_{\mathrm{m}}$, as shown in Fig. 2. In normal OSDM, the DM consists of a pilot vector of length M and the message of size $(N-1) \times M$. In D-OSDM, the DM consists of a pilot vector of length M, U message matrices of size $P \times M$, and $U+1$ zero matrices of size $2Q \times M$ ($P, Q, U \in \mathbb{Z}^+$).
(ii) Read DM in a row-wise direction and obtain a sequence of length MN, $\boldsymbol{x}_{\mathrm{m}}$.
(iii) Apply a transformation matrix $\boldsymbol{F}_N \otimes \boldsymbol{I}_M$ on $\boldsymbol{x}_{\mathrm{m}}$ and obtain a signal block $\boldsymbol{x}$ as:

$$\boldsymbol{x} = \boldsymbol{x}_{\mathrm{m}} \left(\boldsymbol{F}_N \otimes \boldsymbol{I}_M\right). \tag{1}$$

(iv) Insert L zeros (L represents the discrete maximum delay spread and $L \in \mathbb{Z}^+$) to $\boldsymbol{x}$ to avoid inter-block interference.
(v) Up-convert the baseband signal to a passband signal.

The transmitted signal reaches the receiver through the UWA channel by undergoing many effects, such as delay spread, Doppler spread, and noise. Fig. 3 shows a block diagram of normal OSDM and D-OSDM at the receiver. The received signal is processed as follows:

(vi) Synchronize the received signal to correct for the nominal delay and Doppler shift.
(vii) Down-convert the passband signal to the baseband and obtain a received sequence of length MN, $\boldsymbol{y}$, by an overlap-add operation. In normal OSDM, the relationship between $\boldsymbol{x}_{\mathrm{m}}$ and $\boldsymbol{y}$ becomes

$$\boldsymbol{y}\left(\boldsymbol{F}_N^* \otimes \boldsymbol{I}_M\right) = \boldsymbol{x}_{\mathrm{m}} \operatorname{diag}\left(\boldsymbol{C}_{0,0}, \boldsymbol{C}_{1,0}, \ldots, \boldsymbol{C}_{N-1,0}\right), \tag{2}$$

where $\boldsymbol{F}_N^*$ and $\boldsymbol{C}_{n,0}$ ($n = 0, 1, \ldots, N-1$) represent the conjugate transpose of $\boldsymbol{F}_N$ and a matrix of size $M \times M$ containing the channel delay spread, respectively. Eq. (2) means that the mutual orthogonality among pilot and data signals is preserved if the channel can be modeled as a discrete-time model with maximal delay spread L.

In D-OSDM, the relationship between $\boldsymbol{x}_{\mathrm{m}}$ and $\boldsymbol{y}$ becomes

$$\boldsymbol{y}\left(\boldsymbol{F}_N^* \otimes \boldsymbol{I}_M\right) = \boldsymbol{x}_{\mathrm{m}} \sum_{q=-Q}^{Q} \operatorname{diag}\left(\boldsymbol{C}_{0,q}, \boldsymbol{C}_{1,q}, \ldots, \boldsymbol{C}_{N-1,q}\right) \boldsymbol{Z}_{MN}^{Mq}, \tag{3}$$

where $\boldsymbol{C}_{n,q}$ and $\boldsymbol{Z}_{MN}$ represent a matrix of size $M \times M$ containing the channel delay spread at Doppler shift q and a cyclic shift matrix of size $MN \times MN$, respectively. Eq. (3) means that the mutual orthogonality among pilot and data signals is still preserved if the channel can be modeled as a basis expansion model (BEM) [12], whose (discrete) maximal delay and Doppler spreads are L and Q, respectively.
(viii) Analyze the received pilot signal by solving the first M rows of Eqs. (2) and (3) and derive the UWA channel and its related delay spread (normal OSDM) or delay–Doppler spread (D-OSDM).
(ix) Equalize the received signal by solving the remaining rows of Eqs. (2) and (3) using the derived UWA channel.

2.2. Characteristics of normal OSDM and D-OSDM

In this section, we first describe the differences in the redundancy present in D-OSDM and normal OSDM signals. The characteristics of D-OSDM are then revealed by comparing D-OSDM and D-OFDM [11]. Note that D-OFDM is a well-known UWA communication scheme that is robust to Doppler spread and effectively cancels intercarrier interference. D-OFDM is a very suitable benchmark since it has a signal structure comparable to that of D-OSDM.

Fig. 4 shows the structures of normal OSDM, D-OSDM, and D-OFDM in the time–frequency domain under the same block length and bandwidth, where $1/T$ ($T \in \mathbb{R}^+$) is the signal bandwidth. First, the structure of normal OSDM and D-OSDM are focused on (Fig. 4a, b). As shown in the figure, in normal OSDM and D-OSDM, every symbol (i.e., element of the pilot and data signals) appears as a Dirac comb that contains N pulses with period M and M pulses with period N in the time and frequency domain, respectively. This means that the pilot and data vectors appear periodically in both time and frequency, and every symbol is mapped on a lattice in the time–frequency domain that is a sampling the time and frequency axes at intervals N and M, respectively.

As shown in Fig. 4, the data capacity of D-OSDM is smaller than that of normal OSDM (1/3 in the figure) when they are compared under the same block length and bandwidth. This is because D-OSDM uses guardbands between the pilot and data signals in order to measure the delay and Doppler spreads of the UWA channel simultaneously at the receiver side. Normal OSDM does not use guardbands, resulting in a larger data capacity in exchange for a higher Doppler sensitivity. We evaluated the efficiency of normal OSDM and D-OSDM in the following experiments.

The structures of D-OSDM and D-OFDM are focused on next (Fig. 4b, c). As shown in the figure, both D-OSDM and D-OFDM have MN subcarriers with guardbands. In D-OFDM, each element of the pilot and data signal appears only once in the frequency domain. This means that D-OFDM is sensitive to a channel for which a specific subcarrier may suffer from deep fading, since the information transmitted on a subcarrier that is experiencing deep fading may be lost due to the low signal-to-noise ratio (SNR) on that subcarrier. In contrast, D-OSDM intentionally disperses the pilot and data signals over different subcarriers to exploit the

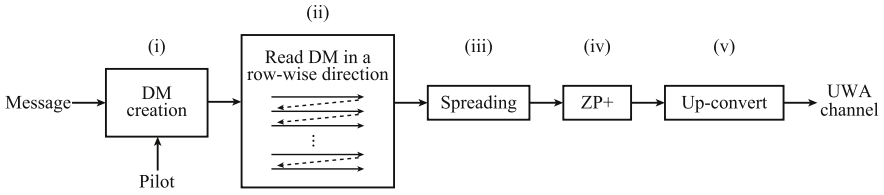

Fig. 1. Transmitter block diagram of normal OSDM and D-OSDM.

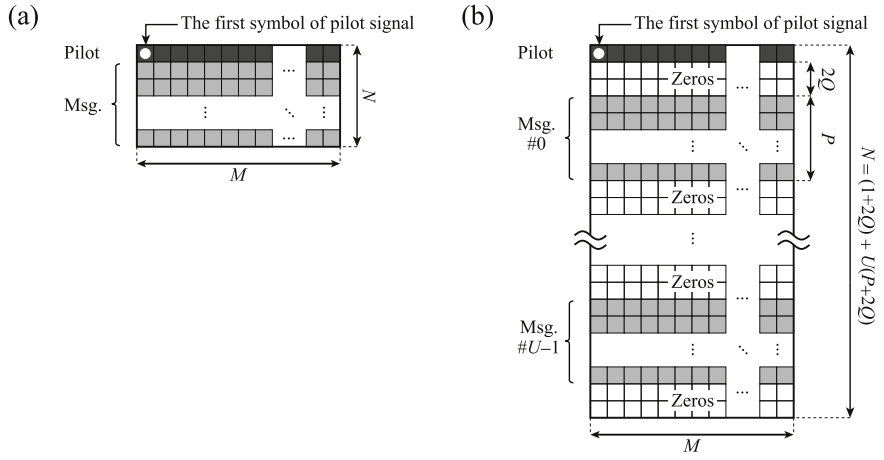

Fig. 2. Structure of data matrix (DM), $\boldsymbol{X}_{\mathrm{m}}$; (a) normal OSDM and (b) D-OSDM.

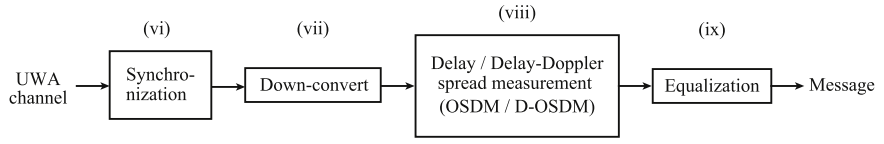

Fig. 3. Receiver block diagram of normal OSDM and D-OSDM.

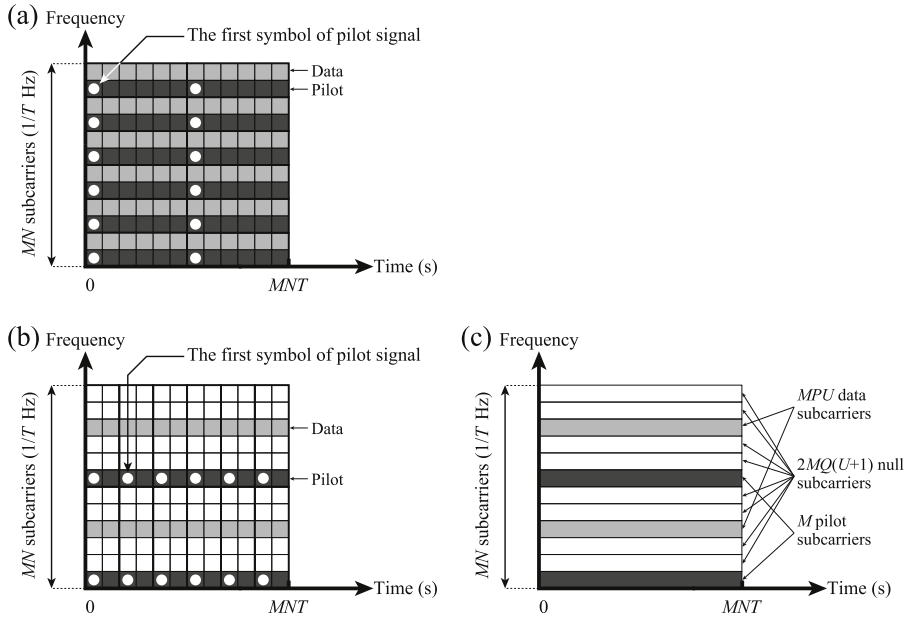

Fig. 4. Structures of (a) normal OSDM, (b) D-OSDM and (c) D-OFDM in the time–frequency domain under the same block length and bandwidth ($M = 6$ and $N = 2$ in normal OSDM, and $M = 2$, $P = 1$, $Q = 1$, $U = 1$ in D-OSDM and D-OFDM).

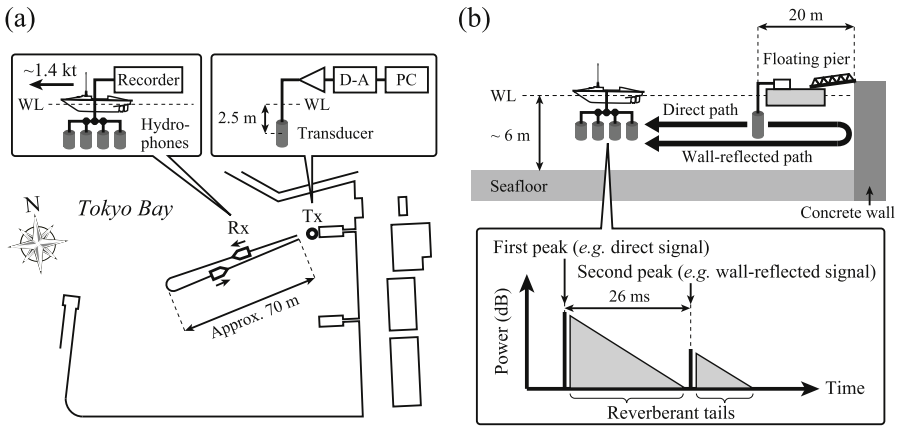

Fig. 5. Testing environment. (a) Top view and (b) side view.

full diversity of the channel. Thus, when the performances of D-OSDM and D-OFDM were compared in channels with large delay and Doppler spreads, the communication quality of D-OSDM was found to be better than that of D-OFDM [10]. In addition, the peak-to-average power ratio of D-OSDM is much smaller than that of D-OFDM, in exchange for receiver complexity. We evaluated the efficiency of D-OSDM and D-OFDM in the following experiments.

3. Experimental setup

A demonstration of normal OSDM, D-OSDM, and D-OFDM for UWA communication was performed in an actual sea environment (in a harbor with a moving receiver). Such conditions will help us understand the practical performance and effectiveness of normal OSDM, D-OSDM, and D-OFDM when they face large delay and Doppler spreads. We also measured the harbor UWA channel and modeled it to better understand its channel characteristics and to confirm the experimental results.

3.1. Experimental environment

Fig. 5 is a map of the experimental site. The experiment was conducted in Hashirimizu, Kanagawa, Japan on June 21, 2016. Throughout the experiment, the weather was rainy, and the sea state was calm (glassy). During the test, there was no strong interference source (e.g., existence of other vessels) or variation in the testing conditions.

As illustrated, the transmitter (Tx) was fixed on a floating pier, and it consisted of a personal computer (PC), a digital-to-analog (D-A) converter, an amplifier, and an omnidirectional transducer (Table 1). The transducer had a transmitting sensitivity of 147.1 dB re. 1 μPa/V@1 m (at 35 kHz), and was located 2.5 m below the water level (WL). The receiver (Rx) was mounted on a remote-controlled boat equipped with a global positioning system (GPS) (RC-S1, Coden), and consists of four hydrophones and two linear pulse-code-modulation (PCM) recorders (Table 1). The maximum input (signal saturation) level and resolution (in terms of digital signal processing) of the Rx were 198.2 dB re. 1 μPa (at 35 kHz) and 144 dB, respectively. Fig. 6 shows the hydrophone locations on the remote-controlled boat. As shown in the figure, four hydrophones were placed at a distance of 0.42–0.45 m, approx. 10 times larger than the wavelength at a carrier frequency of 35 kHz, in order to make the channel impulse response obtained at each hydrophone independent.

In this experiment, the Tx transmitted a communication signal whose carrier frequency was 35 kHz periodically, and the Rx recorded the signal continuously. When the signal transmission started, the remote-controlled boat (with the Rx) departed the pier

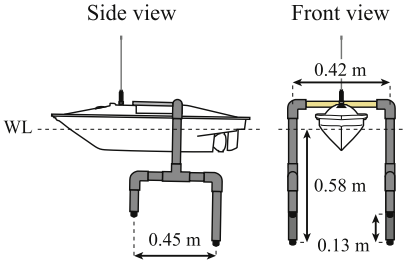

Fig. 6. Hydrophone setting on the remote-controlled boat.

Table 1
Specifications of the transmitter and receiver.

	Component	Specifications
Tx	PC	CF-RX3 (Panasonic)
	D-A converter	USB-6366 (National Instruments)
	Amplifier	HSA4052 (NF Corp.)
	Transducer	OST-2120 (OKI Seatec)
Rx	Hydrophone	H2a (Aquarian Audio Products)
	Linear PCM recorder	PCM-M10 (Sony Corp.)

to the central area of the port (70 m away from the pier), and returned to the pier with a constant speed of 1.4 kt (0.7 m/s). The movement of the remote-controlled boat resulted in a Doppler spread with a various energy per bit to noise power spectral density ratio (E_b/N_0).

Focusing on the UWA channel, there is a line of sight between the Tx and Rx (Fig. 5b). Specifically, there is a direct path from the Tx to the Rx, and a wall-reflected path from the Tx to the Rx via the concrete wall located at the right-hand side in the figure. Considering the sound velocity in water (approx. 1500 m/s), the time difference between the direct path signal and the wall-reflected path signal is 26 ms. These two signals will not be affected by a Doppler spread (the effect of the Doppler shift due to the movement of the remote-controlled boat will be canceled by the synchronization process at the receiver), and the two signals will be observed as a sharp peak in the frequency spectrum at the carrier frequency. In addition, the transmitted signal from the Tx reaches the Rx with reflections from both the sea surface and the sea floor, resulting in a reverberant tail that was observed in the channel impulse response. These reflecting signals have changing Doppler scales due to the movement of the remote-controlled boat, and they will be observed as a spread factor in the frequency spectrum around the carrier frequency. Consequently, the delay spread of the harbor UWA channel will be observed as

Table 2
Parameter settings for the experiments.

Case	Type	Parameters		Performances	Transmission level
#0	D-OSDM	M	63	Block length (ms): 1995	183.3
		P	1	Signal bandwidth $1/T$ (kHz): 1.2	(dB re. 1 μPa@1 m)
		Q	9		
		U	1		
		L	60		
	D-OSDM	M	63	Block length (ms): 36.5	
		P	1	Modulation: QPSK ($b_{\text{bit}} = 2$)	
		Q	1	Code rate c_{rate}: 1 (Coding: N/A)	
		U	1	Data rate (kbps): 0.34	
		L	60	Signal bandwidth $1/T$ (kHz): 1.2	183.3
#1	OSDM	M	189	Block length (ms): 36.5	(dB re. 1 μPa@1 m)
		P	1	Modulation: QPSK ($b_{\text{bit}} = 2$)	
		Q	0	Code rate c_{rate}: 1/3 (Coding: Turbo)	
		U	1	Data rate (kbps): 0.34	
		L	60	Signal bandwidth $1/T$ (kHz): 1.2	
#2	D-OSDM and D-OFDM	M	63	Block length (ms): 36.5	185.3 (1st)
		P	1	Modulation: 16QAM ($b_{\text{bit}} = 4$)	183.0 (2nd)
		Q	1	Code rate c_{rate}: 1 (Coding: N/A)	181.5 (3rd)
		U	1	Data rate (kbps): 0.69	(dB re. 1 μPa@1 m)
		L	60	Signal bandwidth $1/T$ (kHz): 1.2	
#3	D-OSDM and D-OFDM	M	63	Block length (ms): 36.5	185.3
		P	1	Modulation: 16QAM ($b_{\text{bit}} = 4$)	(dB re. 1μPa@1 m)
		Q	1	Code rate c_{rate}: 4/5 (Coding: RS)	
		U	1	Data rate (kbps): 0.55	
		L	60	Signal bandwidth $1/T$ (kHz): 1.2	

shown in Fig. 5b: the direct signal (without Doppler spread), the wall-reflected signal (without Doppler spread), and other reflected signals as reverberation tails (with Doppler spread). This model can support the experimental results, as will be demonstrated later on.

3.2. Flow of the experiment

In this experiment, four cases (cases #0, #1, #2 and #3) were considered. We performed case #0 to measure the harbor UWA channel. Cases #1–#3 were performed to illustrate the advantages of D-OSDM. Specifically, the performance of D-OSDM was compared to that of normal OSDM and D-OFDM with respect to communication quality under fair circumstances (the same data rate and signal bandwidth).

- In case #0, the harbor UWA channel characteristics (delay spread, Doppler spread, and noise) were measured. As a probing signal, we used a D-OSDM signal, whose parameters were optimized for channel probing.
- In case #1, the performances of normal OSDM and D-OSDM were compared.
- In case #2, the performances of D-OSDM and D-OFDM were compared.
- In case #3, the performances of D-OSDM and D-OFDM (both with channel coding) were compared. As the channel coding technique, we used a Reed–Solomon (RS) code (code rate: 4/5).

3.2.1. Signal modulation

Before the experiment, we constructed the communication signals on a software-defined modulator using the parameters shown in Table 2. Fig. 7a shows the time–frequency structure of the D-OSDM signal used for probing (case #0). As shown in the figure, there were 18 guardbands between the pilot and data subcarriers, and 60 zero symbols were inserted between the block signals. By using this probing signal, a maximum Doppler spread of nine subcarriers (4.5 Hz) could be measured with a resolution of 0.5 Hz, and a maximum delay spread of 60 symbols (50 ms) with a resolution of 0.83 ms was observed.

Table 3
Signal specifications for cases #2 and #3.

Boat operation	1st	2nd	3rd
Total no. of bits before encoding	99,994	113,904	111,384
Channel coding	RS	N/A	N/A
No. of transmitting bits	124,992	113,904	111,384

The information in the cyan-colored area and yellow-colored area was used to evaluate the performance of D-OSDM and D-OFDM without channel coding (case #2) and with channel coding (case #3), respectively.

Fig. 7b shows the structure of the normal OSDM (case #1) and D-OSDM signal (cases #1–#3) in the time–frequency domain. Because the signal bandwidth of the two signals is equalized, the data capacity of D-OSDM is 1/3 compared to that of normal OSDM, as described above in Section 2.2. Thus, to compare normal OSDM and D-OSDM under the same data rate, we used a powerful channel coding technique (Turbo code of rate 1/3) for normal OSDM.

Fig. 7c shows the structure of the D-OFDM signal (cases #2 and #3) in the time–frequency domain. By comparing panel (b) in Fig. 7 (in case of D-OSDM) and Fig. 7c, it is clear that the data rate and signal bandwidth of D-OSDM and D-OFDM are all equal.

3.2.2. Signal transmission

As described above in Section 3.1, during the experiment the Tx transmitted the signaling frame periodically and the Rx recorded the signal continuously. The signal received from each hydrophone and the position of the Rx obtained by GPS were stored so that the measurement results can be merged with the position of the Rx.

In case #0, the Tx transmitted a D-OSDM signal (for probing) continuously during the boat operation. During the signal transmission, a silent interval of 1.5 s was inserted every 30 s for the measurement of the noise.

In case #1, the Tx first transmitted a D-OSDM signal continuously during the boat operation. Once the boat returned to the pier, the Tx switched to transmit a normal OSDM signal, and the boat operation was performed again. In this experiment, 516 blocks (65,016 bits) of information were transmitted in each trial (normal OSDM and D-OSDM communication).

In case #2, the Tx first transmitted a D-OSDM signal continuously during the boat operation. This boat operation was repeated

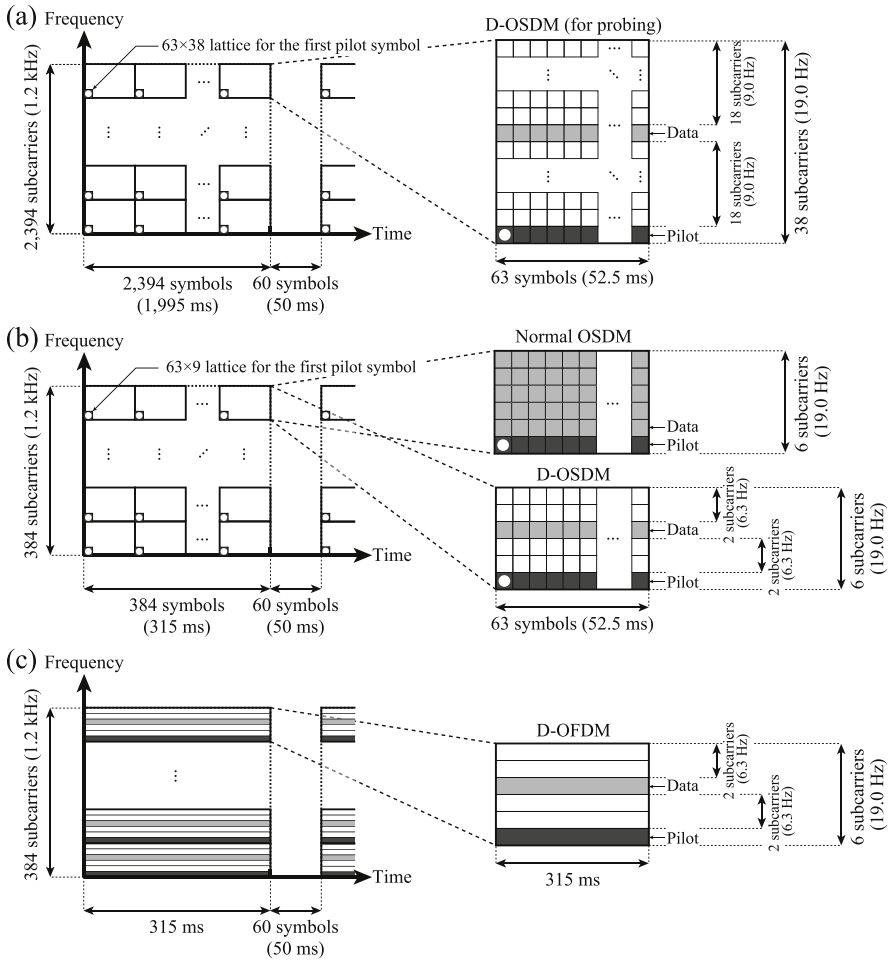

Fig. 7. Structures of communication signals in the time–frequency domain used in the experiments. (a) D-OSDM for probing, (b) normal OSDM and D-OSDM, and (c) D-OFDM.

three times, by changing the transmission level (Table 2). As shown in Table 3, the transmitted symbols in the first operation were encoded by an RS code. However, by bypassing the RS decoding process in the signal demodulation and comparing the transmitted symbols directly (the cyan-colored area in Table 3), the performance without channel coding can be evaluated. Once the above operation was finished, the Tx switched to transmit a D-OFDM signal and the same operation was performed again. In this experiment, 1390 blocks (350,280 bits) of information were transmitted in each trial (D-OSDM and D-OFDM communication).

In case #3, we used the received signal obtained in case #2, where the message was encoded by an RS code (only in the first boat operation). Unlike case #2, the performance with channel coding can be evaluated by adopting the RS decoding process in the signal demodulation and comparing the symbols before encoding and after decoding (yellow-colored area in Table 3). In this case, 496 blocks (99,993 bits before RS encoding) of information were transmitted in each trial (D-OSDM and D-OFDM communication).

3.2.3. Signal demodulation

In case #0, we analyzed only the pilot signal, in order to measure the delay and Doppler spreads of the harbor UWA channel. We also analyzed the received signal of the silent interval to measure the background noise of the harbor UWA channel.

In cases #1–#3, off-line processing was performed on the recorded signal, and the E_b/N_0 and BER were obtained as follows. The received signal was first roughly synchronized to cancel the effect of the Doppler shift caused by the movement of the remote-controlled boat. Note that a Doppler spread remained even after the Doppler shift correction. After this Doppler synchronization step, the received signal was divided into signal blocks, and signal demodulation using normal OSDM, D-OSDM, and D-OFDM was performed on each block. Although the Rx was equipped with four hydrophones, three signals were used for demodulation. We thus calculated four BER and E_b/N_0 values (the number of combinations of three signals out of four) block-by-block, by dividing the number of bit errors by the total number of transmitted bits, and by dividing the power of the signal interval by that of the silent interval, respectively. In other words, there were enough blocks to analyze: 2064 blocks (260,064 bits) for case #1, 5560 blocks (1,401,120 bits) for case #2, and 1984 blocks (399,972 bits) for case #3.

4. Experimental results

4.1. Probing result of the harbor UWA channel (case #0)

4.1.1. Delay spread

We firstly analyzed the characteristics of the UWA channel in terms of delay spread. Fig. 8a shows the relationship between the Tx–Rx distance and the channel impulse response obtained by probing. The channel impulse response had a large delay spread (up to 50 ms) due to a signal reflection from the sea surface and sea bottom. In addition, two peaks that appear regardless of the distance between the Tx and Rx were observed. It will be shown later that these two peaks correspond mainly to the direct path and wall-reflected path in Fig. 5b.

Fig. 8b shows the relationship between the power of the channel impulse response (first peak) and the Tx–Rx distance obtained

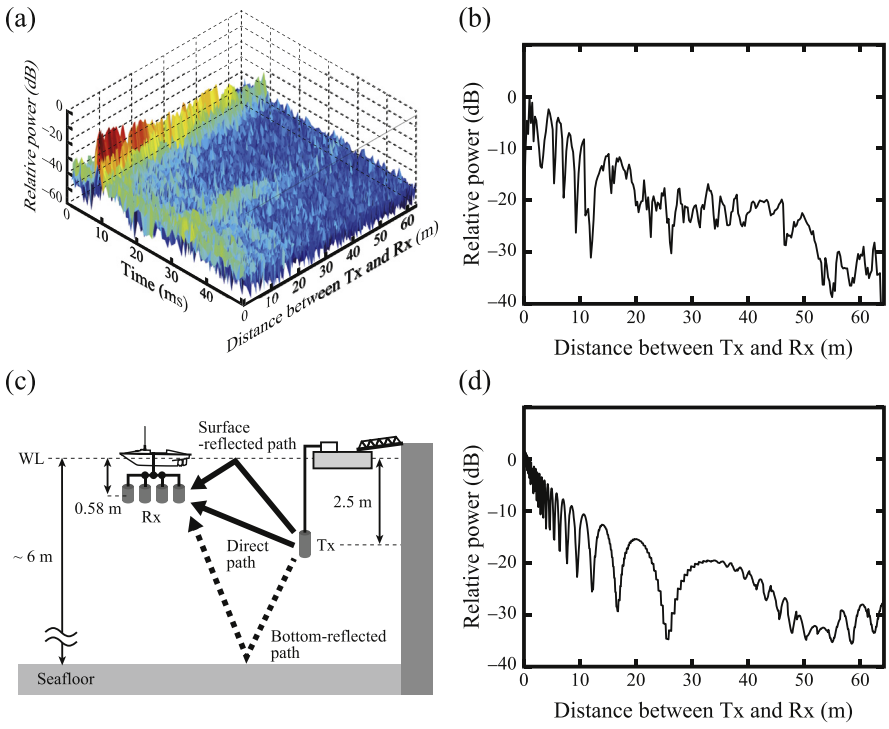

Fig. 8. Relationship between (a) the channel impulse response and the Tx–Rx distance obtained by probing, (b) the power of the channel impulse response (first peak) and the Tx–Rx distance obtained by probing, (c) the channel model to calculate the interference among the direct and reflected paths, and (d) the power of the channel impulse response (first peak) and Tx–Rx distance obtained from the model.

by probing. The power of the first peak decreased as the Tx–Rx distance increased, and it became −30 dB at a distance of 65 m (0 dB at the distance of 0 m). Several notches were also observed. This is due to the interference between the direct signal and the surface-reflected signal. To clarify this, we simulated the signal interference using a simplified UWA channel model. Fig. 8c shows the channel model used to calculate the interference between the direct signal and surface-reflected signal. The signal was assumed to be a short sinusoidal signal (frequency: 35 kHz, signal length: 0.83 ms) whose bandwidth was the same as that of the communication signal (1.2 kHz). In this model, only an interference between the direct signal and surface-reflected signal is considered, since the bottom-reflected signal and wall-reflected signal arrive late and they do not affect the first peak when the Tx–Rx distance is within 70 m. Fig. 8d shows the relationship between the Tx–Rx distance and the power of the channel impulse response (first peak) obtained from the model. As shown in the figure, several notches were observed, similar to the experimental results. This illustrates that the first peak contains the direct signal as well as the surface-reflected signal, which interfere with each other.

Fig. 9 shows the channel impulse response obtained by probing when the Tx–Rx distance was 0–7.5 m. As shown in the figure, two peaks (that appear regardless of the Tx–Rx distance in Fig. 8a), are clearly observed at the times of 6.7 and 31.7 ms. Considering the sound velocity in water (approx. 1500 m/s), this time difference corresponds to a path-length difference of 37.5 m. Because the round-trip distance between the Tx and the concrete wall is approx. 40 m, these two peaks correspond mainly to the direct path and the wall-reflected path in Fig. 5b. Two reverberant tails were also observed following the first and second peak, respectively. As shown in the figure, the power of these reverberant tails changes randomly, due to the random interference among reflected signals.

4.1.2. Doppler spread

Fig. 10a shows an example of the delay–Doppler channel response obtained by probing (case #0). The relative Doppler shift

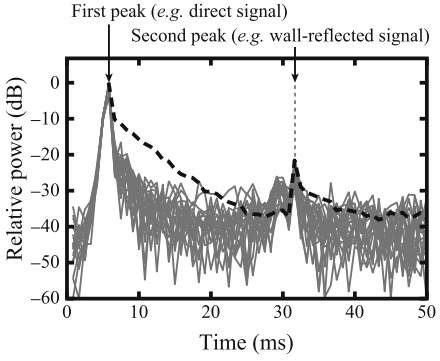

Fig. 9. The channel impulse response obtained by probing when the Tx–Rx distance was 0–7.5 m (solid line) and the average gain of the channel impulse response used in the simulations (dotted line).

(the discretized subcarrier distance in cases #1–#3) is also shown. A large Doppler spread (up to 4.5 Hz) was observed. Because the sea state was calm and the sea surface was glassy throughout the experiment, this Doppler spread was caused mainly by the movement of the Rx. In addition, the first peak in the time domain (direct signal) has a peak at a Doppler shift of 0 Hz as well as a large spread. This is because the first peak contains the direct signal and the surface-reflected signal, with and without Doppler spread, respectively, as described above in Section 4.1.1.

Fig. 10b shows the Doppler power spectrum obtained by probing. A striking feature of the spectrum is the sharp peak, centered at 0 Hz, with a width of approx. 0.5 Hz. This is due to the existence of the direct path from the Tx to the Rx and the wall-reflected path from the Tx to the Rx via the concrete wall. Note that the signal that propagates via these paths will not be affected by Doppler effects, and a sharp peak is observed in the frequency spectrum at the carrier frequency. On the other hand, this spectrum also contains

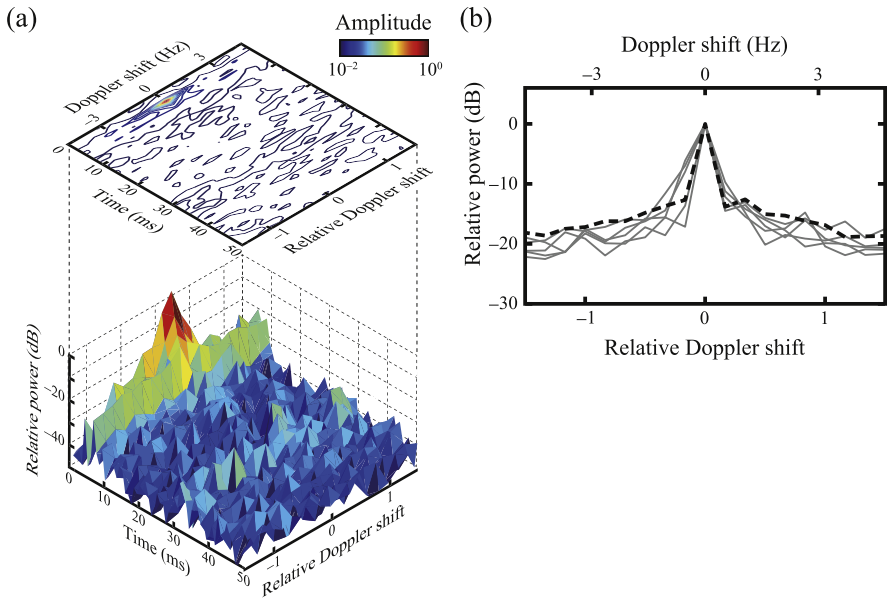

Fig. 10. An example of (a) the delay–Doppler channel response obtained by probing and (b) the Doppler power spectrum obtained by probing (solid line) and the average gain of the Doppler power spectrum used in the simulations (dotted line).

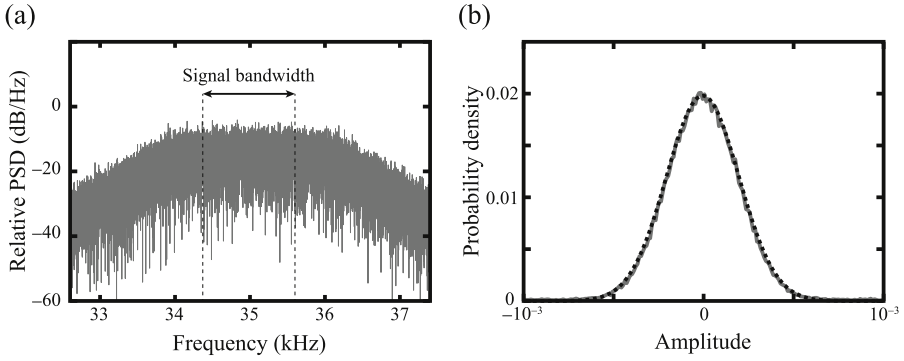

Fig. 11. An example of (a) power spectral density of the background noise obtained by probing and (b) its amplitude distribution obtained by probing (solid line) and that used in the simulations (dotted line, $\sigma = 2.0 \times 10^{-4}$).

spreading components, due to the existence of numerous reflecting paths from the Tx to the Rx.

4.1.3. Noise

Fig. 11a, b shows an example of the power spectral density of the background noise and its amplitude distribution obtained by probing. The power spectral density was almost flat in the signal bandwidth, and the amplitude distribution has a Gaussian shape. This means that the noise in the harbor UWA channel can be modeled as white Gaussian noise.

4.2. Modeling of the harbor UWA channel

To confirm the experimental results, we established a harbor UWA channel model by using the following facts described above in Section 4.1:

- The harbor UWA channel has a delay spread of 50 ms, which corresponds to 60 symbols. The channel impulse response has two peaks, which correspond mainly to the direct path and the wall-reflected path. Reverberant tails exist after the first and second peaks.
- The harbor UWA channel has also a Doppler spread of up to 4.5 Hz. The signal that propagates via the direct path and wall-reflected path will not be affected by Doppler effects. On the other hand, the signal that propagates via the numerous reflecting paths from the Tx to the Rx is affected by Doppler effects.
- The noise in the harbor UWA channel can be modeled as white Gaussian noise.

We therefore modeled the harbor UWA channel by combining two propagation models: (1) a two-path Rayleigh fading channel without Doppler spread to represent the direct path and the wall-reflected path, and (2) a multi-path Rayleigh fading channel with Doppler spread to represent reverberant tails. Fig. 9 (dotted line) and Fig. 10b (dotted line) show the average gain of the channel impulse response and that of the Doppler power spectrum used in the simulations. As the Doppler-spread profile, the bell-shaped function (using function parameter $A = 9$ [13]) with a maximum Doppler shift of 5 Hz was used. The signal powers that propagate over the two-path model and the multi-path model are assumed to be equal. In addition, the background noise is assumed to be white Gaussian noise. Note that this model is almost the same as the one used to represent a test-tank with a surface wave proposed in [10], except for the shape of the Doppler spread (test-tank: Gaussian, harbor: bell-shape). When simulations are performed to confirm the experimental results, this model can support those results, as

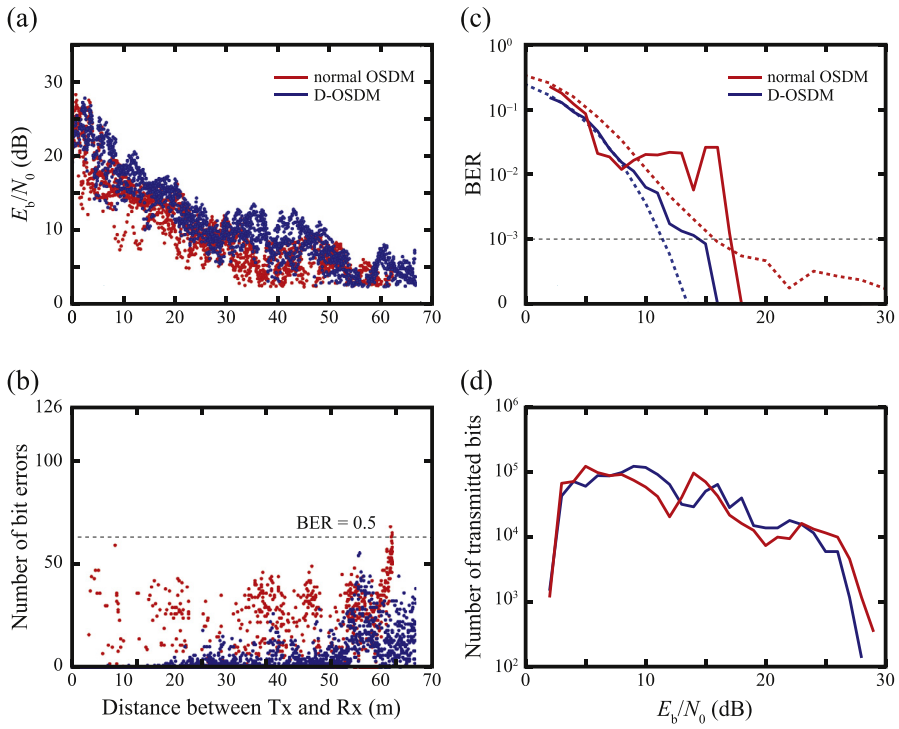

Fig. 12. The relationship between (a) E_b/N_0 and the Tx–Rx distance obtained in the experiment, (b) the number of bit errors and the Tx–Rx distance obtained in the experiment, (c) the BER and E_b/N_0 (solid line: experiment, dotted line: simulation) and (d) the number of transmitted bits and the E_b/N_0 obtained in the experiment.

we demonstrate below. Thus, the channel model of the test-tank considered in our previous work can model the actual system's behavior, and the test-tank environment is suitable to represent the harbor UWA channel environment.

4.3. Comparison of the performances of D-OSDM and normal OSDM (case #1)

Fig. 12 shows the experimental results for the comparison of D-OSDM and normal OSDM. Focusing on the relationship between the E_b/N_0 and the Tx–Rx distance (as shown in Fig. 12a), the E_b/N_0 slightly decreases as the Tx–Rx distance increases, and the E_b/N_0 values of D-OSDM and normal OSDM are almost the same. Fig. 12b shows the relationship between the number of bit errors and the Tx–Rx distance. By comparing the number of bit errors and the E_b/N_0, we observed that the number of bit errors of normal OSDM is larger than that of D-OSDM, although normal OSDM uses a powerful channel coding technique.

Fig. 12c (solid line) shows the relationship between BER and the E_b/N_0. This figure was obtained by calculating the mean BER within a specific range of E_b/N_0 values (0 to 30 dB, every 1 dB). As shown in the figure, D-OSDM achieved no error when the E_b/N_0 was >15 dB, whereas normal OSDM had a BER of 10^{-2} when the E_b/N_0 was around 15 dB. This characteristic (bit errors remain even at large E_b/N_0 values when Doppler spread exists) agrees with the simulation and the test-tank experimental results from our previous study [10]. In addition, this experimental result was also supported by our simulation using the model established above in Section 4.2. As for the simulation results (Fig. 12c, dotted line), D-OSDM achieved a BER of 10^{-3} when the E_b/N_0 was 12 dB, whereas normal OSDM achieved the same BER when the E_b/N_0 was 16 dB.

Fig. 12d shows the number of transmitted bits at each E_b/N_0 (the denominator of each BER in Fig. 12c). As shown in this figure, the number of transmitted bits exceeded 10^4 when the E_b/N_0 was around 15 dB. Because the transmission of 3×10^3 bits without any error gives a 95% confidence level that the true BER is under 10^{-3} [14], the received bits are enough to compare the performance of normal OSDM and D-OSDM at a BER of 10^{-3}.

Consequently, we found that D-OSDM outperforms normal OSDM in a channel with large delay and Doppler spreads.

4.4. Comparison of the performances of D-OSDM and D-OFDM

4.4.1. Without channel coding (case #2)

Fig. 13 shows the experimental results for the comparison of D-OSDM and D-OFDM without channel coding. As described above in Section 4.3, Fig. 13a shows the relationship between the E_b/N_0 and the Tx–Rx distance. The E_b/N_0 slightly decreases as the Tx–Rx distance increases, and the E_b/N_0 of D-OSDM and D-OFDM are almost the same. Fig. 13b illustrates the relationship between the number of bit errors and the Tx–Rx distance in D-OSDM and D-OFDM, respectively. Unlike the results described in Section 4.3, it seems that there is no significant difference between D-OSDM and D-OFDM in Fig. 13. This is because the relationship between the BER of D-OSDM and D-OFDM and the E_b/N_0 is almost the same when they are compared under small E_b/N_0 values. We show below that D-OSDM achieves a better performance than D-OFDM when they are compared under a high E_b/N_0 regime.

Fig. 13c (solid line) shows the relationship between the BER and the E_b/N_0. Now the performance difference between D-OSDM and D-OFDM becomes clear; as shown in the figure, D-OSDM achieves a BER of 10^{-3} when the E_b/N_0 is 20 dB, whereas D-OFDM has a BER floor of 2×10^{-3} when the E_b/N_0 is <30 dB. This means that D-OSDM achieves a far better BER performance if the UWA communication is performed under a high E_b/N_0 regime, and D-OSDM can significantly reduce the signal power required for communications to achieve the same BER, compared to the latest OFDM technique. This experimental result was also supported by simulation using the model established in Section 4.2. As for the simulation results (Fig. 13c, dotted line), D-OSDM achieves a BER of 10^{-3} when the E_b/N_0 is 19 dB, whereas D-OFDM has a BER floor of 10^{-3} when the E_b/N_0 is >25 dB.

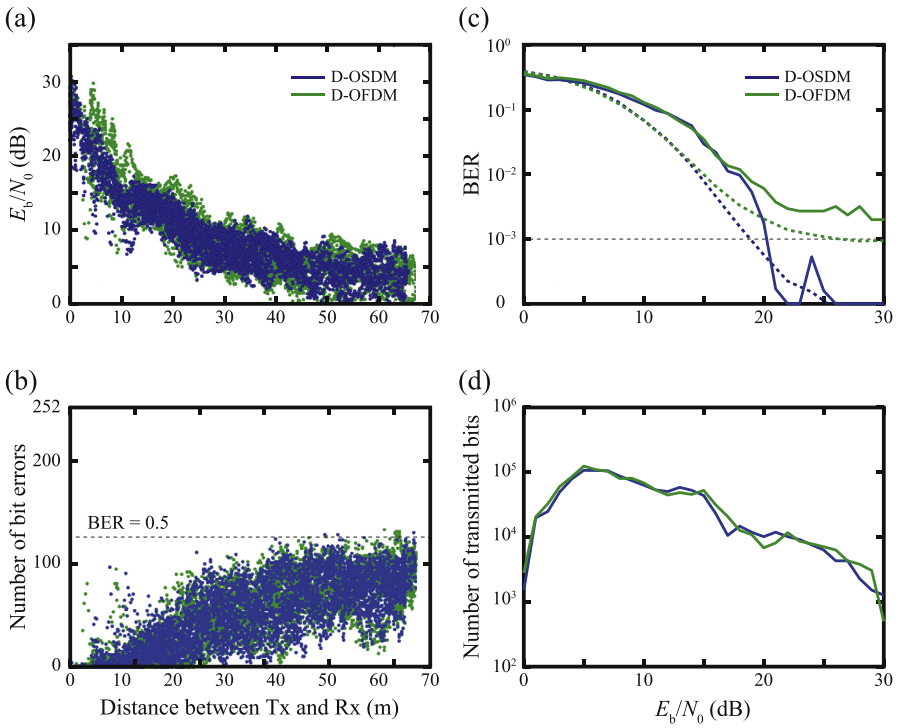

Fig. 13. The relationship between (a) E_b/N_0 and the Tx–Rx distance obtained in the experiment, (b) the number of bit errors and the Tx–Rx distance obtained in the experiment, (c) the BER and E_b/N_0 (solid line: experiment, dotted line: simulation) and (d) the number of transmitted bits and the E_b/N_0 obtained in the experiment.

Moreover, Fig. 13d shows the number of transmitted bits of D-OSDM and D-OFDM at each E_b/N_0 (the denominator of each BER in Fig. 13c). As shown in this figure, the number of transmitted bits exceeds 10^4 when the E_b/N_0 is around 20 dB, and this is enough to compare the performance of D-OSDM and D-OFDM at a BER of 10^{-3}.

We thus observed that D-OSDM outperforms D-OFDM under a high E_b/N_0 regime, if their performances are compared without other techniques, such as channel coding.

4.4.2. With channel coding (case #3)

Fig. 14 shows the experimental results for the comparison of D-OSDM and D-OFDM with channel coding. The relationship between the E_b/N_0 and the Tx–Rx distance (Fig. 14a) is the same as that in case #2 (Fig. 13a), except that we focused on only the first trial result. Fig. 14b illustrates the relationship between the number of bit errors and the Tx–Rx distance in D-OSDM and D-OFDM. By comparing Fig. 14b and Fig. 13b, it is not easy to confirm the effect of channel coding; however, we show below that the performance of both D-OSDM and D-OFDM improves with the use of channel coding and that D-OSDM still outperforms D-OFDM.

Fig. 14c (solid line) shows the relationship between the BER and the E_b/N_0. It is now clear that the performance of both D-OSDM and D-OFDM improves by using channel coding and that D-OSDM still outperforms D-OFDM, as shown in the figure, D-OSDM achieves a BER of 10^{-3} when the E_b/N_0 is 19 dB, whereas D-OFDM achieves the same BER when the E_b/N_0 is around 21 dB. This means that D-OSDM still achieves a slightly better BER performance even when channel coding is used.

This experimental result was also supported by our simulation using the model established above in Section 4.2. As for the simulation results (Fig. 14c, dotted line), D-OSDM achieved a BER of 10^{-3} when the E_b/N_0 was 18 dB, whereas D-OFDM achieved the same BER when the E_b/N_0 was 21 dB. Moreover, Fig. 14d shows the number of transmitted bits of D-OSDM and D-OFDM at each E_b/N_0 (the denominator of each BER in Fig. 14c). As shown in this figure, the number of transmitted bits exceeds 5×10^3 when the E_b/N_0 is around 20 dB, and this is still enough to compare the performance of D-OSDM and D-OFDM at a BER of 10^{-3}. However, an irregular variation and spikes can be seen in Fig. 14c, and more samples would be necessary to reduce these.

We therefore observed that the advantage of D-OSDM over D-OFDM remains even when their performance is compared with channel coding.

4.5. Discussion

In Sections 4.3 and 4.4, we tested normal OSDM, D-OSDM and D-OFDM in a harbor. The results revealed that a UWA communication link using D-OSDM will deliver excellent reliability even for channels with large delay and Doppler spreads. Our simulation results obtained using the harbor UWA channel model showed the same tendency as the experimental results.

However, we also observed that a difference remained between the simulation and experimental results. This is because the channel model was established using a limited number of factors derived from channel probing, and other factors such as the effects of nonlinear power amplifiers [15], the nonlinearity of piezoelectric transducers [16] and signal scattering by the sea-surface and bubbles [17] were ignored. In addition, a BEM has a small error that can be observed as residual noise at the receiver; further only discretized Doppler shifts are assumed in a BEM channel whereas real channels have a continuous Doppler spectrum. We did not consider such factors in the simulation, resulting in a difference between the simulation and experimental results, although the simulation results follow the experimental results.

In addition, the BER of the RS-coded signal improved only at high E_b/N_0 in both the experiment and simulation (see Section 4.4.2). There are three reasons for this: the use of a large modulation rate (16QAM), the existence of noise from Doppler spread, and the large code rate (4/5). In that experiment, the E_b/N_0 was measured by comparing the signal energy and (environmental)

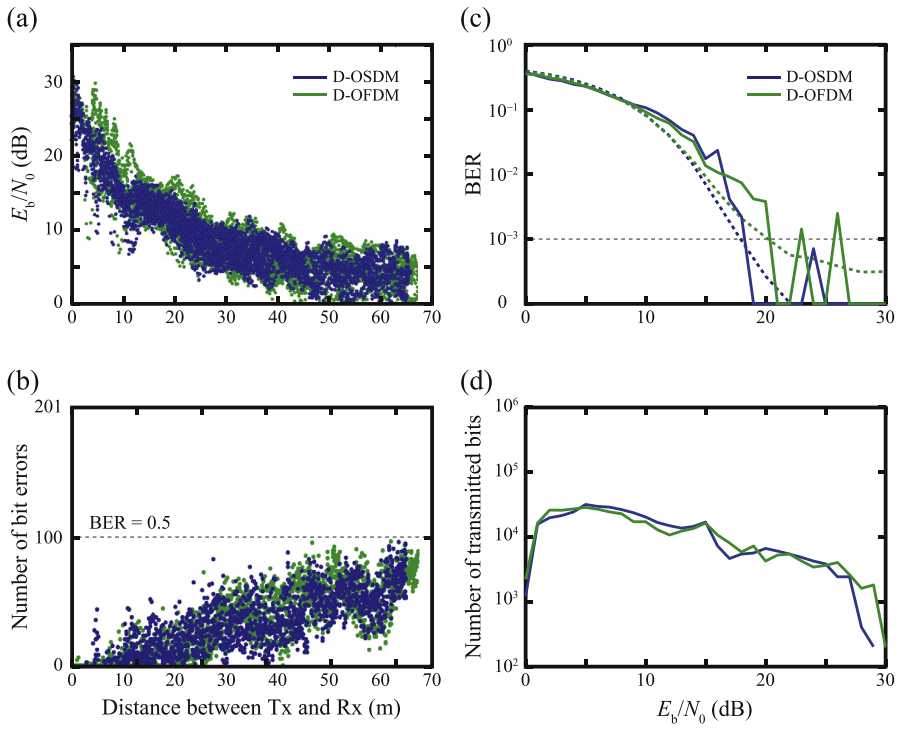

Fig. 14. The relationship between (a) E_b/N_0 and the Tx–Rx distance obtained in the experiment, (b) the number of bit errors and the Tx–Rx distance obtained in the experiment, (c) the BER and E_b/N_0 (solid line: experiment, dotted line: simulation) and (d) the number of transmitted bits and E_b/N_0 obtained in the experiment.

noise energy. However, due to the existence of Doppler spread, inter-carrier interference exists, and this effect was not included as noise energy. In addition, as described in Section 2.1, both D-OSDM and D-OFDM are designed to work in a BEM channel, which has a small error as described above. Thus, at high E_b/N_0, the noise from Doppler spread still exists. In addition, 16QAM is sensitive to noise. Because one redundant bit is added to each block of five bits of useful information in RS-coding (code rate: 4/5), the BER of the RS-coded signal improved only at high E_b/N_0.

5. Conclusions

We conducted this study to perform an initial demonstration of normal OSDM and D-OSDM for UWA communication in a harbor with a mobile receiver. We provided a brief overview of signal processing steps of normal OSDM and D-OSDM and their characteristics in a comparison with existing schemes. The UWA channel characteristics in a harbor with a moving receiver were obtained in experiments, and our findings demonstrated that the harbor UWA channel has a delay spread of 50 ms and a Doppler spread of up to 4.5 Hz, and that the combination of two propagation models can model an actual environment. In addition, UWA communication was performed in a harbor with a moving receiver to help us enhance the practical performance of such a system. In our experiments, D-OSDM achieved far better communication quality compared to the other communication schemes. The simulation results that use the harbor UWA channel model also showed the same tendency as the experimental results.

Overall, it was confirmed that a UWA communication link using D-OSDM will deliver excellent reliability even for channels with large delay and Doppler spreads. These findings will be useful not only for underwater acoustic studies but also for wireless communication systems which face large delay and Doppler spreads, such as vehicle-to-vehicle communication and mobile UWB communication.

Acknowledgments

We thank Prof. Koichi Mizutani, Dr. Naoto Wakatsuki (Faculty of Engineering, Information and Systems, University of Tsukuba), Mr. Satoki Ogiso, Yoshihito Imai, Takuji Kawagishi, Misaki Mito, Hirokazu Iwaya, and Hiromu Tanoi (Graduate School of Systems and Information Engineering, University of Tsukuba) for their help in conducting the experiment. This work was supported by a Grant-in-Aid for Young Researchers (A) from the Japan Society for the Promotion of Science (15H05560).

References

[1] D.W. Matolak, Modeling the vehicle-to-vehicle propagation channel: A review, Radio Sci. 49 (9) (2014) 721–736, 2013RS005363. http://dx.doi.org/10.1002/2013RS005363.
[2] I.R. Capoglu, Y. Li, A. Swami, Effect of doppler spread in OFDM-based UWB systems, IEEE Trans. Wirel. Commun. 4 (5) (2005) 2559–2567. URL http://ieeexplore.ieee.org/xpl/freeabs_all.jsp?arnumber=1532239.
[3] M. Stojanovic, J. Preisig, Underwater acoustic communication channels: Propagation models and statistical characterization, IEEE Commun. Mag. 47 (1) (2009) 84–89. http://dx.doi.org/10.1109/MCOM.2009.4752682.
[4] M. Chitre, S. Shahabudeen, M. Stojanovic, Underwater acoustic communications and networking: Recent advances and future challenges, Mar. Technol. Soc. J. 42 (1) (2008) 103–116.
[5] M. Stojanovic, Recent advances in high-speed underwater acoustic communications, IEEE J. Ocean. Eng. 21 (2) (1996) 125–136. http://dx.doi.org/10.1109/48.486787.
[6] J. Heidemann, M. Stojanovic, M. Zorzi, Underwater sensor networks: applications, advances and challenges, Philos. Trans. R. Soc. Lond. Ser. A Math. Phys. Eng. Sci. 370 (1958) (2011) 158–175. http://dx.doi.org/10.1098/rsta.2011.0214.
[7] T. Ebihara, K. Mizutani, Underwater acoustic communication with an orthogonal signal division multiplexing scheme in doubly spread channels, IEEE J. Ocean. Eng. 39 (1) (2014) 47–58. http://dx.doi.org/10.1109/JOE.2013.2245273.
[8] X.-G. Xia, Precoded and vector OFDM robust to channel spectral nulls and with reduced cyclic prefix length in single transmit antenna systems, IEEE Trans. Commun. 49 (8) (2001) 1363–1374. http://dx.doi.org/10.1109/26.939855.
[9] S. Zhou, G.B. Giannakis, C.L. Martret, Chip-interleaved block-spread code division multiple access, IEEE Trans. Commun. 50 (2) (2002) 235–248. http://dx.doi.org/10.1109/26.983320.

[10] T. Ebihara, G. Leus, Doppler-resilient orthogonal signal-division multiplexing for underwater acoustic communication, IEEE J. Ocean. Eng. 41 (2) (2016) 408–427. http://dx.doi.org/10.1109/JOE.2015.2454411.
[11] Z. Wang, S. Zhou, G.B. Giannakis, C.R. Berger, J. Huang, Frequency-domain oversampling for zero-padded OFDM in underwater acoustic communications, IEEE J. Ocean. Eng. 37 (1) (2012) 14–24. http://dx.doi.org/10.1109/joe.2011.2174070.
[12] A.M. Sayeed, B. Aazhang, Joint multipath-doppler diversity in mobile wireless communications, IEEE Trans. Commun. 47 (1) (1999) 123–132. http://dx.doi.org/10.1109/26.747819.
[13] TGn channel models, IEEE 802.11-03/940r4 (2004-05-10).
[14] J. Redd, Calculating statistical confidence levels for error-probability estimates, Lightwave Mag. 17 (5) (2000) 110–114.
[15] P.K. Singya, N. Kumar, V. Bhatia, Mitigating nld for wireless networks: Effect of nonlinear power amplifiers on future wireless communication networks, IEEE Microw. Mag. 18 (5) (2017) 73–90. http://dx.doi.org/10.1109/MMM.2017.2691423.
[16] D.A. Hall, Review nonlinearity in piezoelectric ceramics, J. Mater. Sci. 36 (19) (2001) 4575–4601. http://dx.doi.org/10.1023/A:1017959111402.
[17] H.S. Dol, M.E.G.D. Colin, M.A. Ainslie, P.A. van Walree, J. Janmaat, Simulation of an underwater acoustic communication channel characterized by wind-generated surface waves and bubbles, IEEE J. Ocean. Eng. 38 (4) (2013) 642–654. http://dx.doi.org/10.1109/JOE.2013.2278931.

Tadashi Ebihara was born in Tokyo, Japan, in 1986. He received the Ph.D. degree from the University of Tsukuba, Tsukuba, Japan, in 2010. He received the Research Fellowship for Young Scientists (DC1), Japan Society for the Promotion of Science (JSPS), 2009–2010. From September 2013 till December 2013 he was a Visiting Professor at the Delft University of Technology, The Netherlands. He is currently an Associate Professor at the Faculty of Engineering, Information and Systems, University of Tsukuba. His research interests include mobile communications and their applications to underwater acoustic communication systems.

Geert Leus was born in Leuven, Belgium, in 1973. He received the electrical engineering degree and the Ph.D. degree in applied sciences from the Katholieke Universiteit Leuven, Belgium, in June 1996 and May 2000, respectively. He has been a Research Assistant and a Postdoctoral Fellow of the Fund for Scientific Research - Flanders, Belgium, from October 1996 till September 2003. During that period, Geert Leus was affiliated with the Electrical Engineering Department of the Katholieke Universiteit Leuven, Belgium. Currently, Geert Leus is a Professor at the Faculty of Electrical Engineering, Mathematics and Computer Science of the Delft University of Technology, The Netherlands. During the summer of 1998, he visited Stanford University, and from March 2001 till May 2002 he was a Visiting Researcher and Lecturer at the University of Minnesota. His research interests are in the area of signal processing for communications. Geert Leus received a 2002 IEEE Signal Processing Society Young Author Best Paper Award and a 2005 IEEE Signal Processing Society Best Paper Award.

Hanako Ogasawara was born in Kochi, Japan. She received the Ph.D. degree from the University of Tsukuba, Tsukuba, Japan, in 2009. She worked as a post-doctoral researcher at Scripps Institution of Oceanography, UC San Diego, 2011–2012. She is currently as a lecturer at National Defense Academy of Japan. Her research topic is underwater acoustic monitoring including ocean acoustic tomography.